Geophysical Research Letters

RESEARCH LETTER
10.1029/2022GL101493

Key Points:

- Winter warm surface temperature anomalies are co-located with melt pond locations in the following summer
- Warm anomalies appear in refrozen leads, in refrozen melt ponds, and in troughs between ridges, due to thinner snow and ice
- We show the potential for prediction of summer melt pond fraction from winter surface temperatures

Supporting Information:

Supporting Information may be found in the online version of this article.

Correspondence to:

L. Thielke,
lthielke@iup.physik.uni-bremen.de

Citation:

Thielke, L., Fuchs, N., Spreen, G., Tremblay, B., Birnbaum, G., Huntemann, M., et al. (2023). Preconditioning of summer melt ponds from winter sea ice surface temperature. *Geophysical Research Letters*, *50*, e2022GL101493. https://doi.org/10.1029/2022GL101493

Received 10 OCT 2022
Accepted 1 FEB 2023

Author Contributions:

Conceptualization: Linda Thielke, Niels Fuchs, Gunnar Spreen
Data curation: Linda Thielke, Niels Fuchs, Gunnar Spreen, Gerit Birnbaum, Marcus Huntemann, Nils Hutter, Polona Itkin, Arttu Jutila, Melinda A. Webster
Formal analysis: Linda Thielke, Niels Fuchs, Bruno Tremblay
Investigation: Linda Thielke
Methodology: Linda Thielke, Gunnar Spreen, Bruno Tremblay
Writing – original draft: Linda Thielke

Preconditioning of Summer Melt Ponds From Winter Sea Ice Surface Temperature

Linda Thielke[1], Niels Fuchs[2,3], Gunnar Spreen[1], Bruno Tremblay[4], Gerit Birnbaum[3], Marcus Huntemann[1], Nils Hutter[3,5], Polona Itkin[6], Arttu Jutila[3], and Melinda A. Webster[7,8]

[1]Institute of Environmental Physics, University of Bremen, Bremen, Germany, [2]Center for Earth System Sustainability, Institute of Oceanography, University of Hamburg, Hamburg, Germany, [3]Alfred Wegener Institute, Helmholtz Centre for Polar and Marine Research, Bremerhaven, Germany, [4]Department of Atmospheric and Oceanic Sciences, McGill University, Montréal, QC, Canada, [5]Cooperative Institute for Climate, Ocean and Ecosystem Studies, University of Washington, Seattle, WA, USA, [6]UiT The Arctic University of Norway, Tromsø, Norway, [7]University of Alaska Fairbanks, Fairbanks, AK, USA, [8]University of Washington, Seattle, WA, USA

Abstract Comparing helicopter-borne surface temperature maps in winter and optical orthomosaics in summer from the year-long Multidisciplinary drifting Observatory for the Study of Arctic Climate expedition, we find a strong geometric correlation between warm anomalies in winter and melt pond location the following summer. Warm anomalies are associated with thinner snow and ice, that is, surface depression and refrozen leads, that allow for water accumulation during melt. Warm surface temperature anomalies in January were 0.3–2.5 K warmer on sea ice that later formed melt ponds. A one-dimensional steady-state thermodynamic model shows that the observed surface temperature differences are in line with the observed ice thickness and snow depth. We demonstrate the potential of seasonal prediction of summer melt pond location and coverage from winter surface temperature observations. A threshold-based classification achieves a correct classification for 41% of the melt ponds.

Plain Language Summary We compare winter surface temperatures from an infrared camera with summer photographs of sea ice with melt ponds. The datasets were recorded from a helicopter during the Multidisciplinary drifting Observatory for the Study of Arctic Climate expedition. Melt ponds form on sea ice in summer when the snow melts and water accumulates in the lower locations on the ice floes. Melt ponds are very important for the Arctic energy budget because they strongly change the sea ice brightness and thus the amount of solar energy absorbed by the ice. We find surface characteristics with similar size and location between warmer areas in winter and the location of melt ponds in summer. For a better process understanding, we calculate the surface temperature with a simple model and find that the warm temperature anomalies are due to thinner ice and snow. Stronger warm temperature anomalies appear in new cracks in the ice which are covered with newly formed, thin ice. With a temperature-based classification, we are able to estimate the summer melt pond fraction.

1. Introduction

Melt ponds on Arctic sea ice are an important component of the summer energy budget (e.g., Nicolaus et al., 2012). Melt water collects at the ice surface during summer melt in topographic lows. Melt ponds contribute to the ice–albedo feedback by lowering the surface albedo (e.g., Curry et al., 1995; Light et al., 2022). For autumn, Anhaus et al. (2021) showed that melt ponds influence light transmission. The preconditioning of melt ponds can be partly explained by ice topography (e.g., Flocco et al., 2015; Polashenski et al., 2012), predominately for deformed second-year ice (SYI), or snow dunes and snow accumulations (Petrich et al., 2012; Polashenski et al., 2012), mainly on level first-year ice (FYI). Additional factors for melt pond preconditioning are ice permeability and pond hydrology (Eicken et al., 2002, 2004). There are distinct differences between melt ponds on level or deformed ice. The melt pond location and size are controlled by the topography of deformed ice while on level ice melt ponds can cover large areas (Webster et al., 2022). The ice topography, induced by ridges or leads, are either remnant from the previous seasons' dynamic events or can be newly created due to ice dynamics and/or snow accumulation (Polashenski et al., 2012). Also, refrozen melt ponds can have a lower ice surface elevation and ice thickness compared to the surroundings. There are still large uncertainties in models to predict melt pond

Writing – review & editing: Linda Thielke, Niels Fuchs, Gunnar Spreen, Bruno Tremblay, Gerit Birnbaum, Marcus Huntemann, Nils Hutter, Polona Itkin, Arttu Jutila, Melinda A. Webster

evolution, especially their parameterization of size, depth, and effect on light transmission (Flocco et al., 2012; Light et al., 2008; Webster et al., 2022).

In the following, we document how anomalies in the winter sea ice surface temperature are connected with melt pond coverage the following summer; opening the door for the use of high-resolution infrared satellite data for seasonal prediction of melt pond fraction (MPF). Higher resolution thermal infrared (TIR) satellites, like Landsat 8, focus to date only on the lower latitudes. We use high-resolution, helicopter-borne surface temperature maps from the Arctic in winter to identify areas of warmer surface temperatures compared to the surroundings (warm anomalies). We strive to gain more knowledge on the preconditioning effects of such anomalies for the next summer's MPF. Surface temperatures in winter are sensitive to the ice and especially snow thickness, which both insulate the surface from the warmer ocean.

Specifically, we present a case study from the observations of the Multidisciplinary drifting Observatory for the Study of Arctic Climate (MOSAiC) expedition from September 2019 to October 2020 (Nicolaus et al., 2022; Rabe et al., 2022; Shupe et al., 2022). RV *Polarstern* (AWI, 2017) drifted with the sea ice from the northern Laptev Sea toward the Fram Strait. This study combines helicopter-borne TIR imaging with optical orthomosaics and topography data from an airborne laser scanner (ALS), snow and ice thickness measurements from ground-based transects, as well as atmospheric measurements of temperature, wind speed, and longwave radiation.

We approximate the location and area of summer melt ponds using the preceding winter's sea ice surface temperature data. Based on the comparison of the helicopter-borne maps, we find warm surface ice temperature anomalies in winter at the location of the next summer's melt ponds. We use a simple one-dimensional thermodynamic model to identify the drivers of the warm anomalies. To conclude, we discuss the potential, limitations, and implications of these novel findings to use them for the improvement of modeling and new ideas for high-resolution satellite remote sensing.

2. Data and Methods

We investigate the same sea ice area several months apart and perform a one-to-one comparison between summer and winter. The main datasets are recorded with helicopter-borne imaging: TIR for the polar night (Thielke et al., 2022b) and optically during the polar day. The rich additional MOSAiC datasets are ideally suited to constrain the physical conditions during the seasons.

2.1. Study Area

The study area (1.3 × 1.3 km) consists of level FYI as well as deformed SYI that survived the previous summer melt (Krumpen et al., 2020). The remnant of the MOSAiC floe observed in summer during leg 4, was during winter (legs 1 and 2) in the deformed ice area at the edge of the main sampling sites (about 1.5 km distance from RV *Polarstern*). The area of the MOSAiC floe in summer is marked by the red polygon in Figure 1.

2.2. Optical Orthomosaic in Summer

We use the optical orthomosaic from 30 June 2020 as the ground truth for the MPF on the MOSAiC floe during summer. The orthomosaic, a composite of aerial RGB images, clearly illustrates the melt ponds as darker grayish-blueish areas in contrast to white ice and the almost black open water around the floe. These optical differences are used in a supervised classification algorithm developed for aerial images of sea ice to semantically divide the orthomosaic into surface type class objects. To reduce the impact of noise on pixel level, the minimum size of the resulting *snow/ice*, *pond*, *submerged ice*, and *open water* objects is limited to 100 pixels at a pixel area of 0.25 m^2 (Fuchs, 2023). The estimated error is below ±2% for the derived MPF.

2.3. Aerial Surface Temperatures in Winter

The surface temperature maps are based on helicopter-borne TIR imaging, performed with the VarioCam HD head 680 camera with a brightness temperature precision of 0.02 K and accuracy of 1 K (Thielke et al., 2022b). We use gridded surface temperatures at 1 m horizontal resolution. We focus on data from 21 January 2020 that contained numerous distinct thermal features. For comparison, we show the warm anomalies in the flight

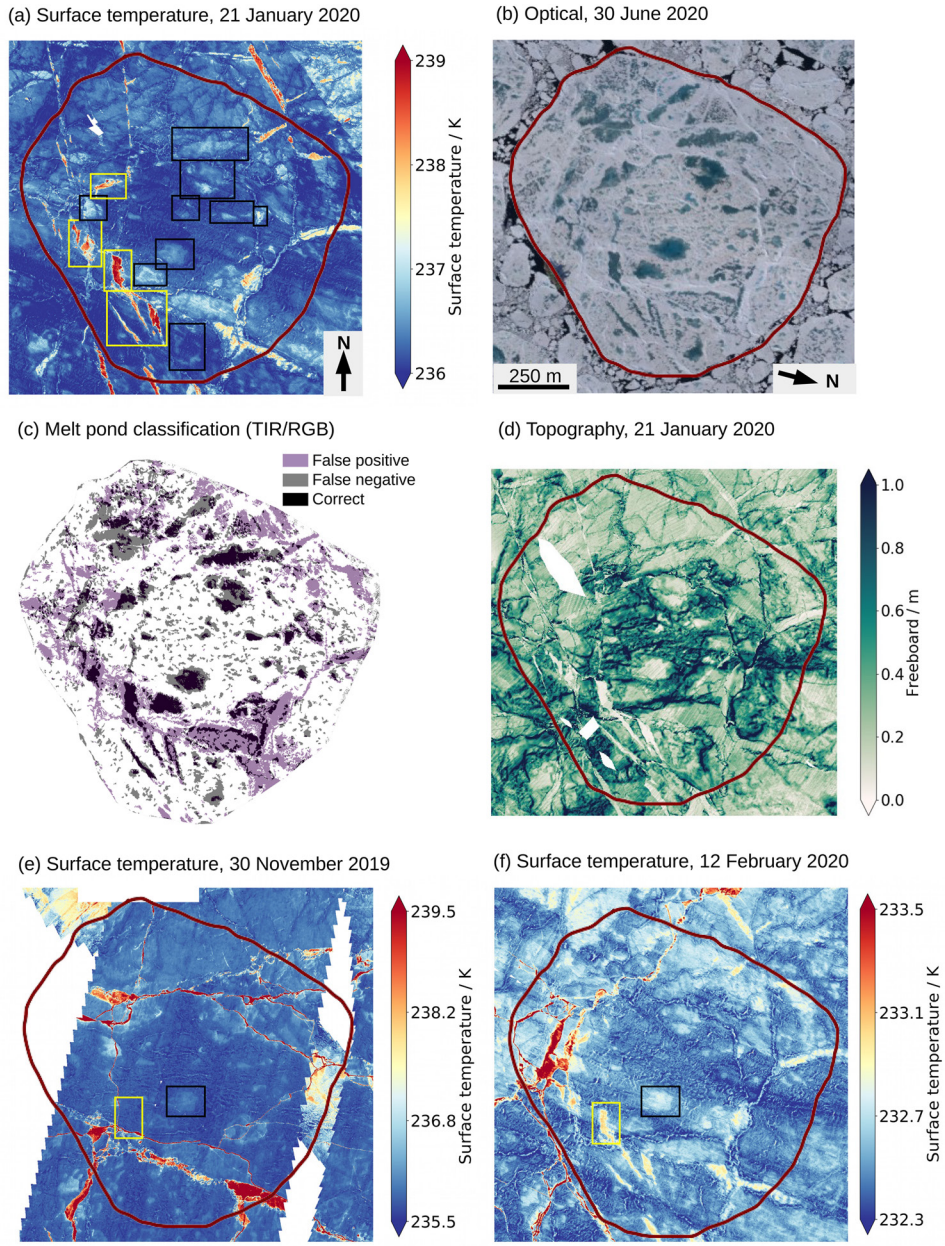

Figure 1. (a) Surface temperature map (TIR) on 21 January 2020 with the boxes indicating the warm anomalies. Yellow boxes are refrozen leads (RL) and black boxes are topography controlled (TC). (b) Optical orthomosaic (RGB) from 30 June 2020 showing the melt ponds as grayish-blueish colors. (c) Overlay of melt pond classification based on a surface temperature threshold on 21 January 2020 and based on RGB classification on 30 June 2020 with fractions of 26% and 22%, respectively. [Purple: only classified by TIR (false positive); Gray: only classified by RGB (false negative); Black: classified in both data (correct).] (d) Freeboard map showing snow surface topography on 21 January 2020. Surface temperatures on (e) 30 November 2019 and (f) 12 February 2020 (note that the colorbar is different for better visibility). The two boxes are indicating the RL and TC cases highlighted in the study. The outline of the summer ice floe as a red polygon for reference.

on 30 November 2019 and 12 February 2020 (Figures 1e and 1f). The temperature anomalies which originate from leads only appeared after end of December 2019 and their temperature signal decreased with time. The topography-driven temperature anomalies vary in the same range of temperature difference in between 30 November 2019 and 12 February 2020. Additional information about the aerial surface temperatures, within the context of the study area, is provided in the Supporting Information S1 (Subsection "Warm temperature anomalies").

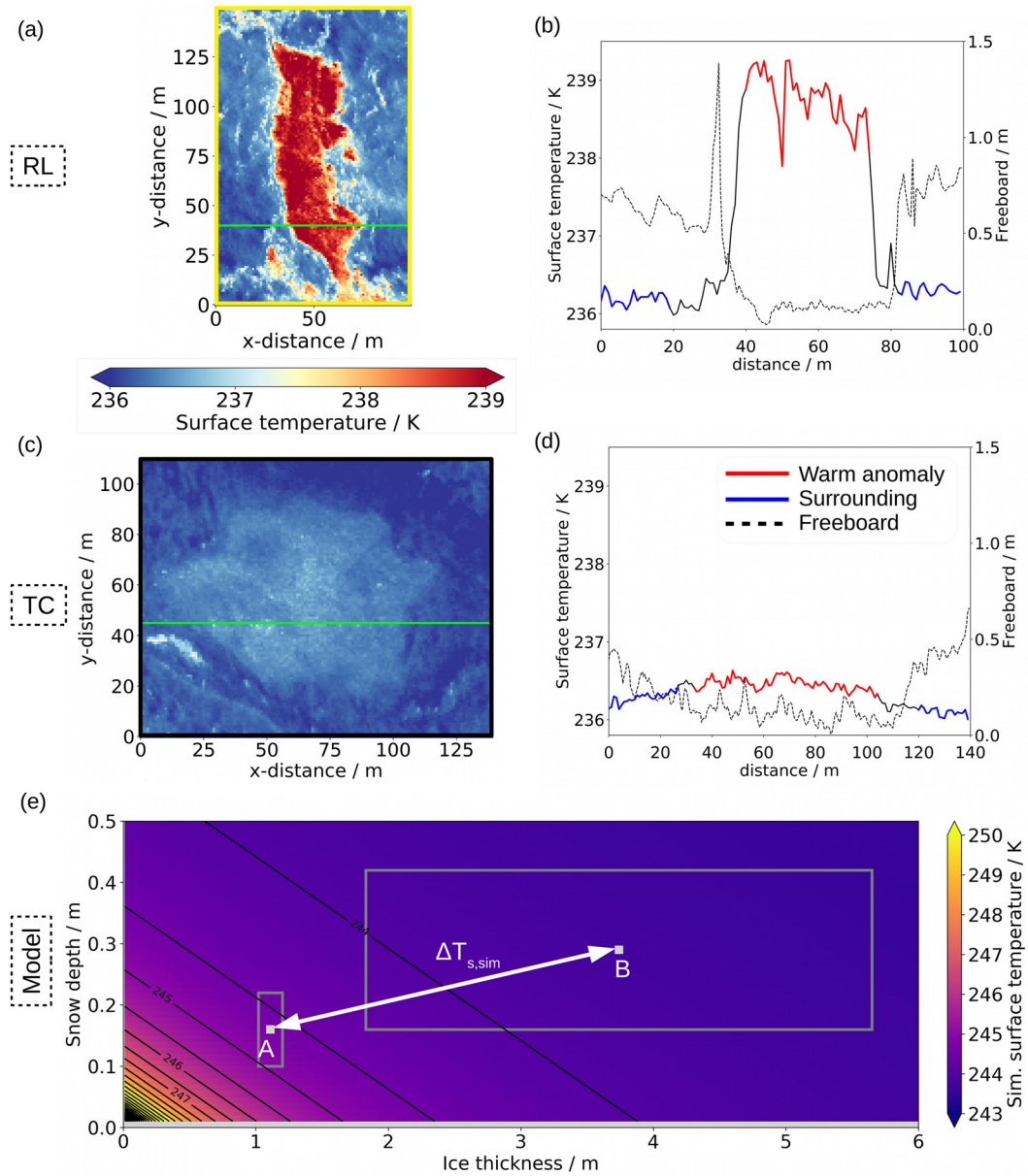

Figure 2. (a, b) Case example for RL (Box 3). (c, d) Case example for TC (Box 5). (a, c) Surface temperature map of the box with a cross-section (green line). (b, d) Surface temperature along the cross-section with the classification of the warm anomaly (red) and the surroundings (blue) and freeboard of the same cross-section (black, dashed). (e) Simulated surface temperature (colored) for ice thickness versus snow depth on 21 January 2020. The black contour lines show the surface temperature step size of 0.5 K. Point "A": typical for the level ice in the warm anomalies; point "B": typical for deformed ice in the surroundings. The boxes are defined based on the mean and standard deviation of the snow and ice thickness.

2.4. Definition of Warm Anomalies

There are two approaches used to define the warm anomalies on the temperature map of 21 January 2020. The first method is more specific to each of the 13 identified cases (boxes in Figure 1a), which is more applicable to the meter scale, while the other is a temperature threshold for identifying warm patches across the 1.5 km floe to perform a melt pond classification.

1. Based on the "ground truth" of the summer optical orthomosaic, we manually defined 13 warm anomalies in the surface temperature map from 21 January 2020. In each box, we analyze two manually selected temperature cross-sections covering both the warm anomaly and the surroundings (Figure 2). We further manually

classify the cross-sections in an "anomaly" and "surrounding" part. The temperatures of the two classes are averaged while the transitions between the two are not analyzed. From that, the surface temperature difference $\Delta T_{s,obs}$ between the two classes is calculated. For the precise definition of the melt pond location, we need a manual classification because the larger scale spatial variability is in the same range as the temperature difference of the warm anomalies.

2. To retrieve the MPF of the whole study area we apply one fixed temperature threshold of 236.35 K to the aerial surface temperature to classify it in melt ponds and ice. The threshold is manually selected by tuning for the most reasonable outcome of the temperature classification compared to the optical ground truth. From this, we can investigate the performance of the winter melt pond classification based on surface temperatures. The classification is very sensitive to the threshold. Varying the temperature threshold between 236.0 and 236.7 K results in a large spread of the classified area ranging from 90% to 10%. Thus, a precise selection of the threshold is crucial. Due to the additional dependence on meteorological conditions, a single generalized threshold is not applicable, but an individual situation-specific tuning could be used. We compare the temperature classification to the classified orthomosaic in terms of location and fraction. Both maps are manually superimposed to achieve the best overlap (Figure 1c).

2.5. Surface Topography

The snow surface topography is retrieved from the ALS, which was operated in the helicopter, parallel to the TIR camera. We use snow freeboard to evaluate the topography of the areas of the warm anomalies and their surroundings as an additional variable for the winter conditions. We consider the relative freeboard due to a possible mean deviation of the ALS derived freeboard data.

2.6. Snow and Ice Conditions

To evaluate the snow and ice conditions, we use measurements along a transect (called "Northern Loop"), which were taken over deformed ice close to our study data. The transect is long enough (about 1.4 km) and covers different ice regimes to represent well the spatial variability of snow depth and ice thickness. More information about the transect location can be found in Figure 2 of Nicolaus et al. (2022). We discriminate between level and deformed ice based on the roughness determined from the 50 m running mean and standard deviation of the ice thickness, same as in Itkin et al. (2023). The level ice thickness is capped at 2 m (assumed thermodynamical growth limit). We use the standard deviation as classification of level ice (<0.2 m) and of deformed ice (>0.6 m). The values of snow and ice thickness measured at the specific transect days (transects were performed monthly to bi-weekly) are fitted polynomially and retrieved for 21 January 2020.

2.7. Thermodynamic Sea Ice Model

We implement a one-dimensional steady-state thermodynamic sea ice model to investigate the sensitivity of the surface temperature to changes in snow and ice thickness as well as atmospheric parameters, that is, 2 m air temperature, 10 m wind speed, and downwelling longwave radiation.

The surface heat budget is defined as (Shokr & Sinha, 2015):

$$F_{\mathrm{LW,down}} - F_{\mathrm{LW,up}} + F_{\mathrm{cond}} - F_{\mathrm{sens}} = 0, \tag{1}$$

where $F_{\mathrm{LW,down}}$ and $F_{\mathrm{LW,up}}$ are the downwelling and upwelling longwave radiation, F_{cond} the conductive heat flux, and F_{sens} the sensible heat flux. Fluxes toward the surface are considered positive. Shortwave radiation is not relevant during winter and the latent heat flux is negligibly small. With the one-dimensional model, we do not consider lateral heat fluxes which we assume to be negligible.

Linearizing $F_{\mathrm{LW,up}}$ using Taylor expansion, the simulated surface temperature $T_{\mathrm{s,sim}}$ is:

$$T_{\mathrm{s,sim}} = \frac{F_{\mathrm{LW,down}} - a + T_{\mathrm{w}}\, d + c\, u\, T_{\mathrm{a}}}{b + c\, u + d}, \quad \text{where} \quad d = \left(\frac{h_{\mathrm{i}}}{k_{\mathrm{i}}} + \frac{h_{\mathrm{s}}}{k_{\mathrm{s}}}\right)^{-1}. \tag{2}$$

T_{w} is the sea water temperature at freezing point, c is the combined sensible transfer coefficient, u the wind speed, h_i is the ice thickness, h_s is the snow depth, k_i and k_s are the thermal conductivity of ice and snow respectively, a and b are the coefficients of linearization.

The model is forced with atmospheric data from the meteorological tower on the floe and longwave radiation from a radiation station, both at the recording time of the surface temperatures. The snow and ice thicknesses of level and deformed ice are taken from the transect data. There can be absolute differences in surface temperature between our observations of TIR surface temperatures and the simulated physical temperature. However, this does not impact relative differences across the floe, which are most important here. The full model descriptions and input parameters can be found in the Supporting Information S1 (Subsection "Details on the thermodynamic model").

3. Results

3.1. Warm Anomaly Types

Comparing the melt ponds from the optical orthomosaic (Figure 1b) with warm anomalies of the surface temperature map in winter (Figure 1a), we find clear similarities in location and shape. Although we did not have any visual appearance of melt ponds in winter and spring, we detected winter temperature anomalies, that became melt ponds in the subsequent summer (boxes in Figure 1a; numbers in Figure S1b in Supporting Information S1).

Based on the observed temperature contrasts and their physical explanation, we define and manually select two types of these warm anomalies:

1. Refrozen leads (RL): newly formed, thin ice in between thicker ice, showing strong positive temperature anomalies.
2. Topography controlled (TC): level ice surrounded by deformed ice, showing weak positive temperature anomalies.

The refrozen leads can be identified easily by their elongated shape and higher surface temperatures due to thinner ice formed after a recent dynamic event. They have a lower surface elevation than the surroundings and potentially collect more snow, which favors melt water collection in summer.

Besides the correlation with the optical orthomosiac, we find the same for areas of low elevation in the topography map from the ALS (Figure 1d). Thus, warm anomalies have thinner ice and snow compared to the surroundings of deformed ice with increased freeboard and surface roughness (also shown in Figures 2b and 2d). Based on this topography data, we can determine TC anomalies although they show a comparatively small temperature difference. Many of the TC anomalies already have the shape of melt ponds and thus potentially were melt ponds already the summer before.

3.2. Local Temperature Differences

We show the results from the manual classification in each box (Table S2 in Supporting Information S1). The surface temperature differences of the two warm anomaly types on 21 January vary between 0.3 and 2.5 K. We find a connection between the temperature difference and the type of anomalies. For the RL (four anomalies), we have a higher temperature difference of 1.7–2.5 K (median = 2.0 K, std = 0.33 K), while the TC anomalies (nine anomalies) have a temperature difference of 0.3–0.7 K (median = 0.4 K, std = 0.17 K).

For simplicity, we focus on one case of each type, RL and TC, because they have a well-distinguishable temperature anomaly. In Figure 2, we show the temperature maps for one RL-case (ΔT_{obs} = 2.5 K) and one TC-case (ΔT_{obs} = 0.3 K) as well as the aligned cross-sections of temperature and freeboard. The cross-sections are classified into warm anomaly (red) and surroundings (blue). The freeboard change is inversely proportional to the temperature change (Figures 2b and 2d). This is consistent with our expectations that the freeboard decreases while the temperature increases, and vice versa. Looking at all helicopter TIR data, we see that RL only appear after the end of December and then the surface temperature difference decreases due to ice growth and potential snow accumulation from 11.8 to 0.5 K. For TC there is no trend with time while it varies at 0.2–1.3 K. The different stages of the warm anomalies on 30 November 2019 and 12 February 2020 are displayed in Figure 1 e and f. Temperature differences of all 13 warm anomalies on 21 January 2020 and in two cases for all 10 helicopter flights between November and February are listed in the Supporting Information S1 (Subsection "Warm temperature anomalies").

3.3. Comparison of Observations and Thermodynamic Model

We compare the warm anomalies from the TIR observation on 21 January 2020 with simulated surface temperature differences, calculated with a steady state one-dimensional thermodynamic model (Section 2.7) to understand

better what is causing the warm winter anomalies. The lower temperature contrast of TC anomalies must be investigated in more detail while for the RL cases it is clear that the newly formed, thinner ice causes the larger temperature differences. Thus, we focus on the TC anomalies on 21 January 2020.

Snow depth and ice thickness from the transect data represent the spatial variability of the study area and show a snow depth of 0.16 m ± 0.06 m for level (A) and 0.29 m ± 0.13 m for deformed ice (B) (Figure 2e). The ice thickness is 1.11 m ± 0.09 m for level ice (A) and 3.74 m ± 1.91 m for deformed ice (B). Based on these representative average values, we implement two regimes of snow depth and ice thickness in our thermodynamic model. The simulated mean temperature difference $\Delta T_{s,sim}$ between the warm anomaly (level) and surroundings (deformed) is 0.88 K with a spread of 0.09–1.47 K (Figure 2e) while 0.30–0.70 K is observed (Section 3.2).

Thus, the thermodynamic model slightly overestimates the temperature anomaly. The simulated temperature difference using the same snow depth for level and deformed ice (0.23 m) would be 0.59 K. Therefore, the effect of variable snow depth accounts for 0.29 K of the 0.88 K in our simulation. But this snow depth variability is quite uncertain based on our limited amount of measurements. On the short spatial and temporal range, the atmospheric conditions are considered constant and do not cause additional variability.

3.4. Temperature-Based Melt Pond Classification

The threshold-based TIR classification is able to approximate the next summer MPF of an ice floe. With a temperature threshold of 236.35 K, applied to the surface temperature map on 21 January 2020, we derive a MPF of 26% (Figure 1c). This is slightly higher than the fraction of 22% for the optical classification on 30 June 2020. With the ponds expanding after the first drainage event in mid-July, however, the optical observations also show a higher fraction of 24% on 22 July 2020. Thus, we are able to partly replicate the summer melt pond classification, already 6 months in advance. This is a first step toward a seasonal prediction of melt ponds. The shortcomings are the uncertainties on level FYI as well as that we are missing smaller melt ponds (melt pond size distribution follows a power law (Huang et al., 2016; Popović et al., 2018)). Also the high spatial variability of the surface temperature influences the classification which is sensitive to small changes in the threshold. The temperature classification performed correctly for 41% of the optical classified ponds (Figure 2c). The remaining 59% are not classified although in summer melt ponds are present (false negative). In relation to the whole surface area of the floe, the fraction of false positive (17% of the floe) and false negative (13% of the floe) are in the same order of magnitude. Therefore, the overall MPF is similar for the TIR and optical classification, which can be a coincidence. However, as 41% of the summer melt ponds are correctly identified in the winter TIR data, that number is the approximate performance of the winter to summer melt pond prediction.

4. Discussion

Studies about melt pond properties (Huang et al., 2016) and photogrammetry of the sea ice topography (Divine et al., 2016) using optical data are limited to the summer season. Helicopter-borne ALS data, available in summer and winter, were also used to explore the role of surface roughness for melt pond presence (Webster et al., 2022). The topography, measured by the ALS, is included to a large extent in the surface temperatures while the surface temperatures contain additionally thermodynamic surface information. Thus, there is high potential to further fuse these two datasets. With high-resolution winter surface temperatures, we add an additional data source for a better understanding of melt pond precursors outside the summer season. We show for the first time that melt pond locations can be already seen in winter temperature anomalies due to the thermodynamic properties of snow and sea ice.

We find areas of refrozen leads or level ice with thinner snow at the location of the surface temperature anomalies and deformed ice in the surroundings. This is reasonable because areas of low elevation tend to turn into melt ponds (Polashenski et al., 2012). The ice topography and snow variability align with the findings of Scott and Feltham (2010) and Holland et al. (2012). Two modes, corresponding to level and deformed ice as found in the transect ice thickness (1.11 and 3.74 m), are also visible in the ice thickness transect performed on 07 January 2020 over parts of the study area (Figure S2 in Supporting Information S1). When we zoom into the study area, these modes are represented also by the ALS freeboard. We can identify modes for each of the anomalies which are below the surroundings (Figure S3 in Supporting Information S1). This strengthens our assumptions for the two ice thickness regimes in the thermodynamic model. Previous studies stated that snow plays an important role

for melt pond formation (Petrich et al., 2012; Scott & Feltham, 2010). In our study, we can confirm the importance of snow: the snow depth is linked to the ice topography, that is, thinner snow is present over level ice and causes warm temperature anomalies (Itkin et al., 2023). During the MOSAiC expedition there was thin snow compared to the climatology which makes the anomalies more emphasized due to less insulation by the snow (Itkin et al., 2023).

The presence of some TC melt ponds coincides with the locations of re-frozen melt ponds from the previous summer. Itkin et al. (2023) shows presence of re-frozen melt ponds in the southern part of the Central Observatory (CO) in October. The size of the warm anomalies over the southern and other parts of CO suggests that the re-frozen melt ponds were wide spread. The re-appearance of melt ponds at the previous season's location was already mentioned before in the context of the Surface Heat Budget of the Arctic Ocean (SHEBA) expedition (Eicken et al., 2001). In one case (Box 4), we find a warmer circle around a colder middle part, which could indicate a bottom-up melt pond from last summer. The trough of the previous melt pond could serve as the melt water collection location and seed the appearance of a melt pond in the next season.

To simulate the surface temperature, we assumed a commonly used value of snow thermal conductivity ($k_s = 0.30$ W m^{-1} K^{-1}, Bitz and Lipscomb (1999)). The model results are sensitive to the thermal conductivity potentially leading to overestimated results. The investigation of the thermal conductivity is an important but large topic itself and out of the scope of this study.

The threshold-based temperature melt pond classification proves its potential in this case study. The threshold must be adapted to different environmental conditions before it can be used further, for example, in models. The absolute surface temperature and its anomaly are affected by atmospheric parameters, such as air temperature and wind speed. Thus a statistical analysis of the surface temperature distribution could be used to find the best threshold. The comparison to the optical classification shows that a single threshold has still some problems to classify melt pond locations correctly. 41% of the summer locations are correctly predicted and thus the majority was not. This shows the limit of our prediction: while 41% is still a useful prediction we cannot expect to identify all summer melt ponds already in winter. However, our comparison does not take sea ice dynamics as well as snow accumulation and redistribution between winter and summer into account. Melt ponds can expand more easily on level ice, which presumably leads to the rather poor performance of our classification on level ice. As stated in the introduction, there are other factors we do not consider, like ice permeability and pond hydrology of different ice types, which will help to develop further constraints for the classification. Thus some of the mismatches might be due to that and can partly explain the good match of the classified overall MPF of 26% in winter and 22% (maximum 24%) in summer.

Regarding the timing of the compared datasets: We compare our winter surface temperature to an advanced melt pond extent (30 June), before the drainage of the melt ponds happened. The mid-winter surface temperatures (21 January) have a large contrast due to very low air temperature and the warmer ocean. We presume that the winter temperature anomalies align best when surface depressions are filled with melt water.

Melt pond schemes in regional and climate models could benefit from our findings: melt ponds should be tracked in models throughout the whole year and not only in summer. This increases the potential for melt pond prediction. So far the ice and snow topography is not represented sufficiently in General Circulation Models (e.g., Flocco et al., 2012). But in this study, we show how important the ice topography and roughness are for melt pond formation, already in winter. Nevertheless, the models have a much coarser spatial resolution and are potentially pan-Arctic. Thus, our results would need to be adapted for larger scales.

Until now, refrozen leads were not considered as an indicator of melt ponds. The refrozen leads can add potential areas for next summer's melt pond formation. Here, we can show that a proper representation of lead formation and ice dynamics is necessary to improve the melt pond prediction. Thus, the area of refrozen leads explains a part of the MPF of the following summer. While sea ice is becoming thinner, it becomes more dynamic, and more leads can form. Thus, there is potential for an increased area of melt ponds in the future, which can alter the albedo of sea ice.

Further, TIR remote sensing data can help to support our findings. Satellites instead of helicopter surveys would be an ideal tool to cover larger areas. However, so far, higher resolution TIR satellite remote sensing is performed only in lower latitudes, while we show their potential benefits for the whole Arctic. Nevertheless, their current spatial resolution of about 100 m is still not sufficient to resolve the warm anomalies, which are usually smaller.

This study should motivate to implement high-resolution TIR satellite-based observations, like the upcoming Copernicus Land Surface Temperature Monitoring mission with 30 m resolution (Koetz et al., 2018), to resolve small-scale physical processes on a wider scale and extend their coverage to polar regions. In addition, our applied methods have to be further developed to have a more automatic application to a variety of datasets.

5. Conclusion

We show that warm surface temperature anomalies over sea ice in winter can be co-located with melt ponds of the following summer. We define two different types of warm anomalies: refrozen leads and topography controlled melt ponds. The warm anomalies of the topography controlled melt ponds are characterized by level ice compared to the deformed surroundings, which means thinner snow and ice for the warm anomalies. With a thermodynamic model, we are able to replicate (with a slight ΔT overestimation) the observed surface temperature difference based on observed snow and ice thickness difference and atmospheric parameters. Thus, we can fully attribute the warm anomaly to the ice and snow cover (and not, e.g., wind-driven effects), which eventually also affects later pond formation. Based on a simple threshold-based classification, we are able to use high-resolution surface temperature in winter as a seasonal prediction tool for the summer MPF. The winter prediction of the observed summer MPF agrees within their uncertainty and 41% of the summer melt pond locations are identified correctly.

As Scott and Feltham (2010) and Landy et al. (2014) point out, there is a need for a better understanding of physical processes influencing melt pond formation and evolution which is driven by meteorological events, ice dynamics, and thermodynamics. The relationships between winter ice surface temperature and melt pond development found here can serve the development of improved melt pond parameterizations in regional and climate models. They should track refrozen lead locations throughout the winter and take pond formation in refrozen leads into account to simulate a more realistic melt pond distribution. As shown in this study, there is a large potential for high-resolution TIR data to study small-scale properties of sea ice, either from airborne platforms like here or hopefully in future satellite missions.

Acknowledgments
This work was supported by the German Ministry for Education and Research (BMBF) as part of the International Multidisciplinary drifting Observatory for the Study of the Arctic Climate (Grant MOSAiC20192020), NiceLAB-pro (Grant 03F0867A), and IceSense (Grants 03F0866B and 03F0866A). We acknowledge the support by the Deutsche Forschungsgemeinschaft (DFG) through the International Research Training Group IRTG 1904 ArcTrain (Grant 221211316), the MOSAiCmicrowaveRS project (Grant 420499875) , and the Transregional Collaborative Research Center TRR 172 (Grant 268020496) "Arctic Amplification: Climate Relevant Atmospheric and Surface Processes, and Feedback Mechanisms (AC)^3". PI was supported by Research Council of Norway (SIDRiFT, Grant 287871). MAW conducted this work under the National Aeronautics and Space Administration's New Investigator Program in Earth Science (80NSSC20K0658) and the National Science Foundation Project (2138786). NH was partially funded by the Cooperative Institute for Climate, Ocean, & Ecosystem Studies (CIOCES) under NOAA Cooperative Agreement NA20OAR4320271, Contribution No 2022-1245. We thank all persons involved in the expedition of the Research Vessel Polarstern during MOSAiC in 2019–2020 (AWI_PS122_00), and especially, HeliService and their pilots (Nixdorf et al., 2021). We also thank for the discussion and support around this project: Philipp Anhaus, Larysa Istomina, Felix Linhardt, Niklas Neckel, and Marcel Nicolaus. We thank the reviewers for the very constructive feedback which helped to improve the manuscript. Open Access funding enabled and organized by Projekt DEAL.

Data Availability Statement

Datasets:

- Optical orthomosaics: https://doi.org/10.1594/PANGAEA.949167 (Fuchs & Birnbaum, 2022).
- Surface temperature maps: https://doi.org/10.1594/PANGAEA.940846 (Thielke et al., 2022a).
- Freeboard map: https://doi.pangaea.de/10.1594/PANGAEA.951010 (Hutter et al., 2022) [dataset in review at time of publication].
- Atmospheric parameter: https://doi.org/10.18739/A2VM42Z5F (Cox et al., 2021) [updated version used].
- Radiation: https://doi.org/10.1594/PANGAEA.952359 (Pirazzini et al., 2022).
- Transect ice thickness: https://doi.org/10.1594/PANGAEA.943666 (Hendricks et al., 2022).
- Transect snow depth: https://doi.org/10.1594/PANGAEA.937781 (Itkin et al., 2021).

Software:

- Optical image classification: https://doi.org/10.5281/zenodo.7548469 (Fuchs, 2023).

References

Anhaus, P., Katlein, C., Nicolaus, M., Hoppmann, M., & Haas, C. (2021). From bright windows to dark spots: Snow cover controls melt pond optical properties during refreezing. *Geophysical Research Letters*, *48*(23), e2021GL095369. https://doi.org/10.1029/2021GL095369

Bitz, C. M., & Lipscomb, W. H. (1999). An energy-conserving thermodynamic model of sea ice. *Journal of Geophysical Research*, *104*(C7), 15669–15677. https://doi.org/10.1029/1999JC900100

Cox, C., Gallagher, M., Shupe, M., Persson, O., Solomon, A., Blomquist, B., et al. (2021). 10-meter (m) meteorological flux tower measurements (level 1 raw), multidisciplinary drifting observatory for the study of Arctic climate (MOSAiC), central Arctic, October 2019 - September 2020 [Dataset]. Arctic Data Center. https://doi.org/10.18739/A2VM42Z5F

Curry, J. A., Schramm, J. L., & Ebert, E. E. (1995). Sea ice-albedo climate feedback mechanism. *Journal of Climate*, 8(2), 240–247. https://doi.org/10.1175/1520-0442(1995)008%3C0240:SIACFM%3E2.0.CO;2

Divine, D. V., Pedersen, C. A., Karlsen, T. I., Aas, H. F., Granskog, M. A., Hudson, S. R., & Gerland, S. (2016). Photogrammetric retrieval and analysis of small scale sea ice topography during summer melt. *Cold Regions Science and Technology*, *129*, 77–84. https://doi.org/10.1016/j.coldregions.2016.06.006

Eicken, H., Grenfell, T., Perovich, D., Richter-Menge, J., & Frey, K. (2004). Hydraulic controls of summer Arctic pack ice albedo. *Journal of Geophysical Research*, *109*(C8), C08007. https://doi.org/10.1029/2003JC001989

Eicken, H., Krouse, H., Kadko, D., & Perovich, D. (2002). Tracer studies of pathways and rates of meltwater transport through arctic summer sea ice. *Journal of Geophysical Research*, *107*(C10), SHE–22. https://doi.org/10.1029/2000JC000583

Eicken, H., Tucker, W., & Perovich, D. (2001). Indirect measurements of the mass balance of summer arctic sea ice with an electromagnetic induction technique. *Annals of Glaciology*, *33*, 194–200. https://doi.org/10.3189/172756401781818356

Flocco, D., Feltham, D. L., Bailey, E., & Schroeder, D. (2015). The refreezing of melt ponds on Arctic sea ice. *Journal of Geophysical Research: Oceans*, *120*(2), 647–659. https://doi.org/10.1002/2014JC010140

Flocco, D., Schroeder, D., Feltham, D. L., & Hunke, E. C. (2012). Impact of melt ponds on Arctic sea ice simulations from 1990 to 2007. *Journal of Geophysical Research*, *117*(C9), C09032. https://doi.org/10.1029/2012JC008195

Fuchs, N. (2023). PASTA-ice Github Repository (v2023.01) [Software]. Zenodo. https://doi.org/10.5281/zenodo.7548469

Fuchs, N., & Birnbaum, G. (2022). Orthomosaics and surface type classifications of MOSAiC Leg 4 floe (2020-06-30, 2020-07-22) [Dataset]. PANGAEA. https://doi.org/10.1594/PANGAEA.949167

Hendricks, S., Itkin, P., Ricker, R., Webster, M., von Albedyll, L., Rohde, J., et al. (2022). GEM-2 quicklook total thickness measurements from the 2019-2020 MOSAiC expedition [Dataset]. PANGAEA. https://doi.org/10.1594/PANGAEA.943666

Holland, M. M., Bailey, D. A., Briegleb, B. P., Light, B., & Hunke, E. (2012). Improved sea ice shortwave radiation physics in CCSM4: The impact of melt ponds and aerosols on Arctic sea ice. *Journal of Climate*, *25*(5), 1413–1430. https://doi.org/10.1175/JCLI-D-11-00078.1

Huang, W., Lu, P., Lei, R., Xie, H., & Li, Z. (2016). Melt pond distribution and geometry in high Arctic sea ice derived from aerial investigations. *Annals of Glaciology*, *57*(73), 105–118. https://doi.org/10.1017/aog.2016.30

Hutter, N., Hendricks, S., Jutila, A., Birnbaum, G., von Albedyll, L., Ricker, R., & Haas, C. (2022). Merged grids of sea-ice or snow freeboard from helicopter-borne laser scanner during the MOSAiC expedition flight 20200121_01, version 1 [Dataset]. PANGAEA. https://doi.pangaea.de/10.1594/PANGAEA.951010

Itkin, P., Hendricks, S., Webster, M., von Albedyll, L., Arndt, S., Divine, D., et al. (2023). Sea ice and snow characteristics from year-long transects at the MOSAiC Central Observatory. *Elementa: Science of the Anthropocene*, *10*(1). https://doi.org/10.1525/elementa.2022.00048

Itkin, P., Webster, M., Hendricks, S., Oggier, M., Jaggi, M., Ricker, R., et al. (2021). Magnaprobe snow and melt pond depth measurements from the 2019-2020 MOSAiC expedition [Dataset]. PANGAEA. https://doi.org/10.1594/PANGAEA.937781

Knust, R. (2017). Polar research and supply vessel POLARSTERN operated by the Alfred-Wegener-Institute. *Journal of Large-Scale Research Facilities*, *3*, A119. Alfred-Wegener-Institut Helmholtz-Zentrum für Polar- und Meeresforschung. https://doi.org/10.17815/jlsrf-3-163

Koetz, B., Bastiaanssen, W., Berger, M., Defourney, P., Del Bello, U., Drusch, M., et al. (2018). High Spatio- temporal resolution Land surface temperature mission—A copernicus candidate mission in support of agricultural monitoring. In *Igarss 2018-2018 IEEE international geoscience and remote sensing symposium* (pp. 8160–8162). https://doi.org/10.1109/IGARSS.2018.8517433

Krumpen, T., Birrien, F., Kauker, F., Rackow, T., von Albedyll, L., Angelopoulos, M., et al. (2020). The MOSAiC ice floe: Sediment-laden survivor from the Siberian shelf. *The Cryosphere*, *14*(7), 2173–2187. https://doi.org/10.5194/tc-14-2173-2020

Landy, J., Ehn, J., Shields, M., & Barber, D. (2014). Surface and melt pond evolution on landfast first-year sea ice in the Canadian Arctic Archipelago. *Journal of Geophysical Research: Oceans*, *119*(5), 3054–3075. https://doi.org/10.1002/2013JC009617

Light, B., Grenfell, T. C., & Perovich, D. K. (2008). Transmission and absorption of solar radiation by Arctic sea ice during the melt season. *Journal of Geophysical Research*, *113*(C3), C03023. https://doi.org/10.1029/2006JC003977

Light, B., Smith, M. M., Perovich, D. K., Webster, M. A., Holland, M. M., Linhardt, F., et al. (2022). Arctic sea ice albedo: Spectral composition, spatial heterogeneity, and temporal evolution observed during the MOSAiC drift. *Elementa: Science of the Anthropocene*, *10*(1), 000103. https://doi.org/10.1525/elementa.2021.000103

Nicolaus, M., Katlein, C., Maslanik, J., & Hendricks, S. (2012). Changes in Arctic sea ice result in increasing light transmittance and absorption. *Geophysical Research Letters*, *39*(24), L24501. https://doi.org/10.1029/2012GL053738

Nicolaus, M., Perovich, D. K., Spreen, G., Granskog, M. A., von Albedyll, L., Angelopoulos, M., et al. (2022). Overview of the MOSAiC expedition: Snow and sea ice. *Elementa: Science of the Anthropocene*, *10*(1), 000046. https://doi.org/10.1525/elementa.2021.000046

Nixdorf, U., Dethloff, K., Rex, M., Shupe, M., Sommerfeld, A., Perovich, D. K., et al. (2021). MOSAiC extended acknowledgement. *Zenodo*. https://doi.org/10.5281/zenodo.5541624

Petrich, C., Eicken, H., Polashenski, C. M., Sturm, M., Harbeck, J. P., Perovich, D. K., & Finnegan, D. C. (2012). Snow dunes: A controlling factor of melt pond distribution on Arctic sea ice. *Journal of Geophysical Research*, *117*(C9), C09029. https://doi.org/10.1029/2012JC008192

Pirazzini, R., Hannula, H.-R., Shupe, M. D., Uttal, T., Cox, C. J., Costa, D., et al. (2022). Upward and downward broadband shortwave and longwave irradiance and downward diffuse and direct solar partitioning during the MOSAiC expedition [Dataset]. PANGAEA. https://doi.org/10.1594/PANGAEA.952359

Polashenski, C., Perovich, D., & Courville, Z. (2012). The mechanisms of sea ice melt pond formation and evolution. *Journal of Geophysical Research*, *117*(C1), C01001. https://doi.org/10.1029/2011JC007231

Popović, P., Cael, B., Silber, M., & Abbot, D. S. (2018). Simple rules govern the patterns of Arctic Sea ice melt ponds. *Physical Review Letters*, *120*(14), 148701. https://doi.org/10.1103/PhysRevLett.120.148701

Rabe, B., Heuzé, C., Regnery, J., Aksenov, Y., Allerholt, J., Athanase, M., et al. (2022). Overview of the MOSAiC expedition: Physical oceanography. *Elementa: Science of the Anthropocene*, *10*(1), 00062. https://doi.org/10.1525/elementa.2021.00062

Scott, F., & Feltham, D. (2010). A model of the three-dimensional evolution of Arctic melt ponds on first-year and multiyear sea ice. *Journal of Geophysical Research*, *115*(C12), C12064. https://doi.org/10.1029/2010JC006156

Shokr, M., & Sinha, N. (2015). *Sea ice: Physics and remote sensing*. John Wiley & Sons.

Shupe, M. D., Rex, M., Blomquist, B., Persson, P. O. G., Schmale, J., Uttal, T., et al. (2022). Overview of the MOSAiC expedition: Atmosphere. *Elementa: Science of the Anthropocene*, *10*(1), 00060. https://doi.org/10.1525/elementa.2021.00060

Thielke, L., Huntemann, M., Hendricks, S., Jutila, A., Ricker, R., & Spreen, G. (2022a). Helicopter-borne thermal infrared sea ice surface temperature maps with 1 m resolution during the MOSAiC expedition, NetCDF format, version 2 [Dataset]. PANGAEA. https://doi.org/10.1594/PANGAEA.940846

Thielke, L., Huntemann, M., Hendricks, S., Jutila, A., Ricker, R., & Spreen, G. (2022b). Sea ice surface temperatures from helicopter-borne thermal infrared imaging during the MOSAiC expedition. *Scientific Data*, *9*(1), 1–16. https://doi.org/10.1038/s41597-022-01461-9

Webster, M. A., Holland, M., Wright, N. C., Hendricks, S., Hutter, N., Itkin, P., et al. (2022). Spatiotemporal evolution of melt ponds on Arctic sea ice: MOSAiC observations and model results. *Elementa: Science of the Anthropocene*, *10*(1), 000072. https://doi.org/10.1525/elementa.2021.000072

References From the Supporting Information

Untersteiner, N. (1964). Calculations of temperature regime and heat budget of sea ice in the central Arctic. *Journal of Geophysical Research*, *69*(22), 4755–4766. https://doi.org/10.1029/JZ069i022p04755

Yu, Y., & Rothrock, D. (1996). Thin ice thickness from satellite thermal imagery. *Journal of Geophysical Research*, *101*(C11), 25753–25766. https://doi.org/10.1029/96JC02242